

S-Pol QC1 Data Quality Processing for PRECIP

Mike Dixon, Ulrike Romatschke, John Hubbert

**Remote Sensing Facility
Earth Observing Laboratory
National Center for Atmospheric Research*
Boulder, Colorado**

2023/03/09

* NCAR is sponsored by the National Science Foundation.

Contents

1. Project time-line	3
2. Calibration issues	5
2.1 Transmitter and clutter power monitoring	5
2.2. Receiver calibration	8
2.3. Noise monitoring to estimate changes in receiver gain	11
2.4. Monitoring using solar scans	13
3. Generating the QC1 data set	17
3.1 Generating the moments data from the time series	17
3.2 Checking the partially-corrected moments data set.	17
3.3 Checking the ZDR calibration using the Z vs ZDR relationship method	19
3.4. Applying further corrections to the moments data	21
3.5. Checking the corrected data set	21
4. Creating the derived fields - Particle ID (PID) and precipitation rate (QC1, Version 1.0)	23
4.1 Running RadxRate	23
4.2. Missing data in RHIs at 101/281 degrees	23
4.3. Creating quick-look images to check the full data set	24
5. Fields in the QC data set CfRadial files	26
6. Procedures followed to create the data set (NCAR internal)	28
7. References	31

1. Project time-line

The NCAR/EOL S-Pol S-band radar operated at the Nanliao site, near Hsinchu, Taiwan, for the duration of the Prediction of Rainfall Extremes Campaign In the Pacific (PRECIP) field project from 2022/05/25 to 2022/08/11.

The radar was installed at the Nanliao site in early May, and was up and running in test mode by May 21, 2022. During the period May 21 to May 24, testing and calibration was carried out, and the system was prepared for 24-hour operations during the field project. The antenna control program was tested with the scans specified by the S-Pol PIs. The scans were a combination of 360-degree PPIs in Surveillance mode, and RHIs.

Formal operations were conducted from 02 UTC on 2022/05/25 to 00 UTC on 2022/08/11.

Table 1.1 below provides the date/time of events of significance for data quality purposes:

Table 1.1: PRECIP operations timeline for S-Pol QC purposes.

Date	Notes
2022/05/24	Initial calibration. Antenna scan testing in progress.
2022/05/25	Project operations begin, pulse width 1.0 us, staggered PRT 2/3 mode, 0.0016/0.0024 sec.
2022/06/01	Transmitter showing signs of slow degradation, an almost linear 0.05 dB per day decrease in power. This is the start of the transmitter pulse shaper problems. Some transmitter adjustments were made. A calibration was performed.
2022/06/11	Some transmitter adjustments were made.
2022/06/12	The transmitter pulse shaper (what we refer to as pulse shaper #0) became unstable, with relatively rapid ~2dB changes in power. Power measured at the top waveguide alternated between 88 and 86 dBm. Continuous transmitter power measurements allowed us to monitor the transmitter power fluctuations. The monitoring data is included in the meta data for both the time series and the moments.
2022/06/13	Pulse shaper #0 problems were diagnosed in more detail.
2022/06/20	Installed loaner NEXRAD pulse shaper #1 from CWB at KWFS.
2022/06/21	Tested and tuned CWB pulse shaper #1. Pulse width 1.5 us, staggered PRT 2/3 mode, 0.0016/0.0024 sec. Transmit power stable at 88.2 dBm at top of transmitter. Receiver calibration performed.
2022/06/23	Receiver calibration.

Date	Notes
2022/07/08	Replaced CWB pulse shaper #1 with reconditioned unit #2 from the NEXRAD reconditioning center. Pulse width 1.5 us, staggered PRT 2/3 mode, 0.0016/0.0024 sec. Transmit power stable at 88.2 dBm. NOTE - the effective pulse width may not have been as long as measured - see later in this report.
2022/07/15	H channel receiver gain shows signs of decreasing by about 0.5 dB. This H channel instability remained for the rest of the project, and became worse over time.
2022/07/16	Receiver calibration.
2022/07/18	Receiver calibration.
2022/07/23	Receiver calibration.
2022/08/03	Receiver calibration.
2022/08/08	H channel receiver gain decreases by another 1.0 dB, for a total decrease of ~1.5 dB from the start of the project.
2022/08/09	Receiver calibration.
2022/08/10	Receiver calibration.
2022/08/11	Project ends. Post-op calibrations.

2. Calibration issues

2.1 Transmitter and clutter power monitoring

Melnikov and Zrnic, 2022, recommended using clutter power monitoring for determining radar stability and checking the calibration . We use clutter analysis to investigate the stability of Z and ZDR during PRECIP.

In order to perform clutter monitoring, we need to use selected clutter targets visible by the radar. Figure 2.1 shows the ‘persistent clutter’ field for S-Pol at PRECIP, as well as the fraction of time these targets were present during a period of observation. The targets in the red region of the right panel are suitable for monitoring since they are present almost all of the time. We consider targets suitable for analysis if they are present over 99% of the time.

Figure 2.1 (a) , below, shows the reflectivity of the observed clutter field at an elevation angle of 1.5 degrees. We use the RadxClutter application to analyze the clutter - Figure 2.1 (b) shows the frequency of the clutter targets over a 6 hour period of time. The red pixels in (b) indicate the gates for which the clutter is reliably present and constant. We monitor the returned power from those gates, in both H and V, to deduce the stability of the reflectivity and clutter ZDR measurements through the project period.

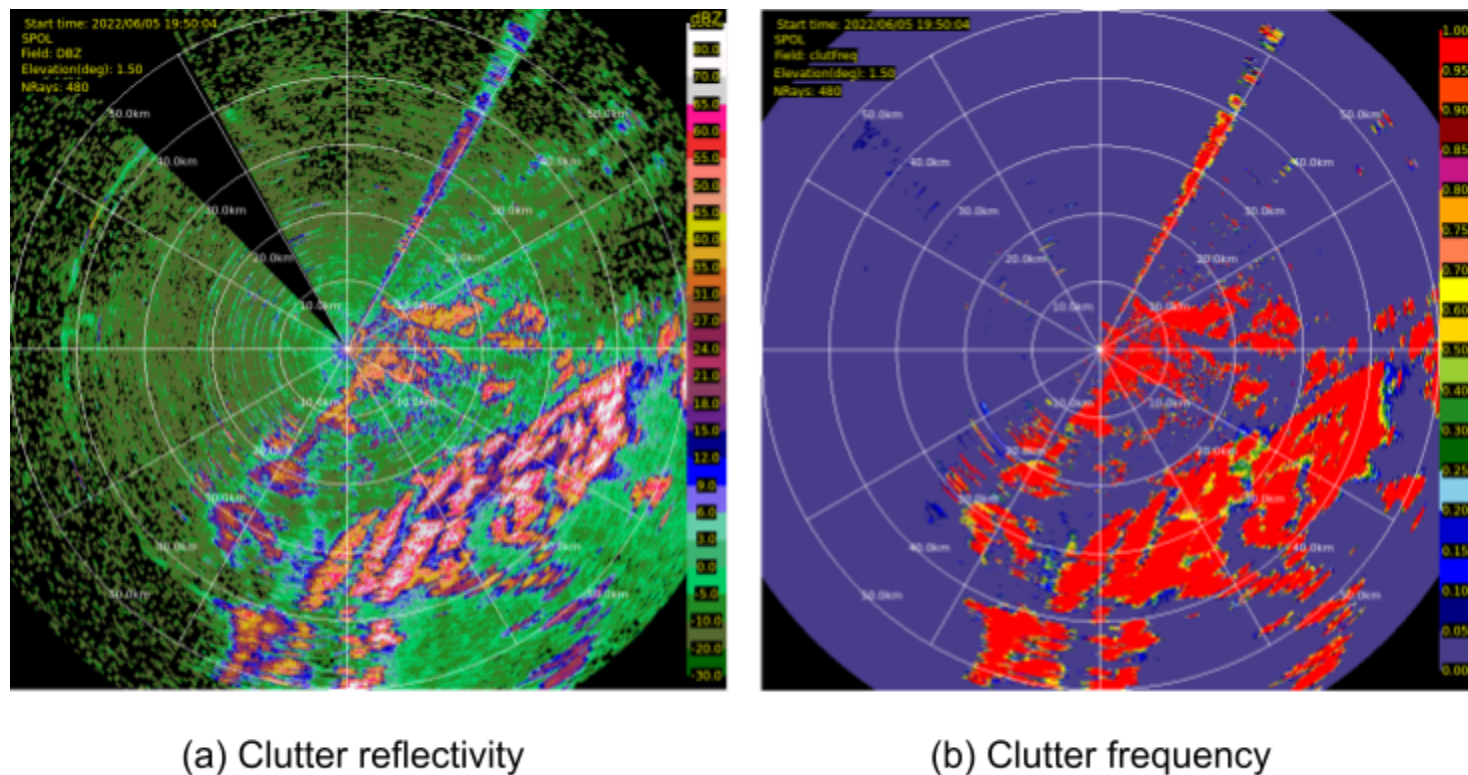


Figure 2.1: measured clutter field at an elevation of 1.5 degrees.

The RadxClutMon application was used to read in the clutter statistics from Figure 2.1, and analyze the returned power in H and V from the clutter targets over the course of the project. From this we can estimate both Z and ZDR from the clutter targets.

We also monitored the transmitter power throughout the project, so that we can correct the reflectivity for fluctuations in transmitter power.

Figure 2.2, below, shows:

- top panel: mean ZDR from clutter targets.
- middle panel: red - mean H clutter power; blue - mean V clutter power; green - mean clutter DBZ.
- bottom panel: transmit power monitoring: black - top of transmitter; red - H channel; blue - V channel.

Also shown in Figure 2.2 are the periods over which each pulse shaper was used:

- pulse shaper #0 - the original from NCAR.
- pulse shaper #1 - the loaner from the CWB.
- pulse shaper #2 - the replacement from the NEXRAD Reconditioning Center.

From Figure 2.2 we can draw the following conclusions:

- Bottom panel - the transmitter power monitoring shows the linear decrease in power over time, for pulse shaper #0, from the start of the project until 2022/06/09. At that time the pulse shaper becomes unstable, with power fluctuations of around 2 dB. These are accurately measured by the power meters.
- After pulse shaper #1 is installed (2022/06/21) the transmitter power stabilizes.
- After pulse shaper #2 is installed (2022/07/09) the measured transmitter power remains stable.
- Middle panel - the clutter power for the H (red) and V (blue) channels tracks the decreasing power from shaper #0, and the measured instability in transmitter power from 2022/06/11 to 2022/06/21. After the installation of shaper #1, the clutter power in H and V is stable. When shaper #2 is installed the clutter power in both H and V decreases by about 0.5 dB. From 2022/07/15 the clutter power in H starts to decrease, and is somewhat unstable thereafter, fluctuating by up to 0.5 dB. On 2022/08/07 the H clutter power drops by a further 1 dB. During this time the V clutter power remains stable. This indicates a problem with the H receiver, and the interpretation is that the H receiver gain decreased and became somewhat unstable.
- Middle panel: the clutter reflectivity (green) remains quite stable during pulse shaper #0 and #1. This indicates that we are correctly adjusting the calibration for the measured power changes. However, when pulse shaper #2 is installed the clutter reflectivity drops by an average of 0.7 dB. This indicates that the effective pulse length for shaper #2 was probably around 1.28 us, rather than the theoretical 1.5 us.
- Top panel - the clutter ZDR is reasonably stable from the start of the project until 2022/07/15. At that time the ZDR of clutter decreases by about 0.5 dB. A further decrease of about 1.0 dB in clutter ZDR is observed on 2022/08/07. This reflects the diagnosis that the H receiver gain decreased in the latter stages of the project.

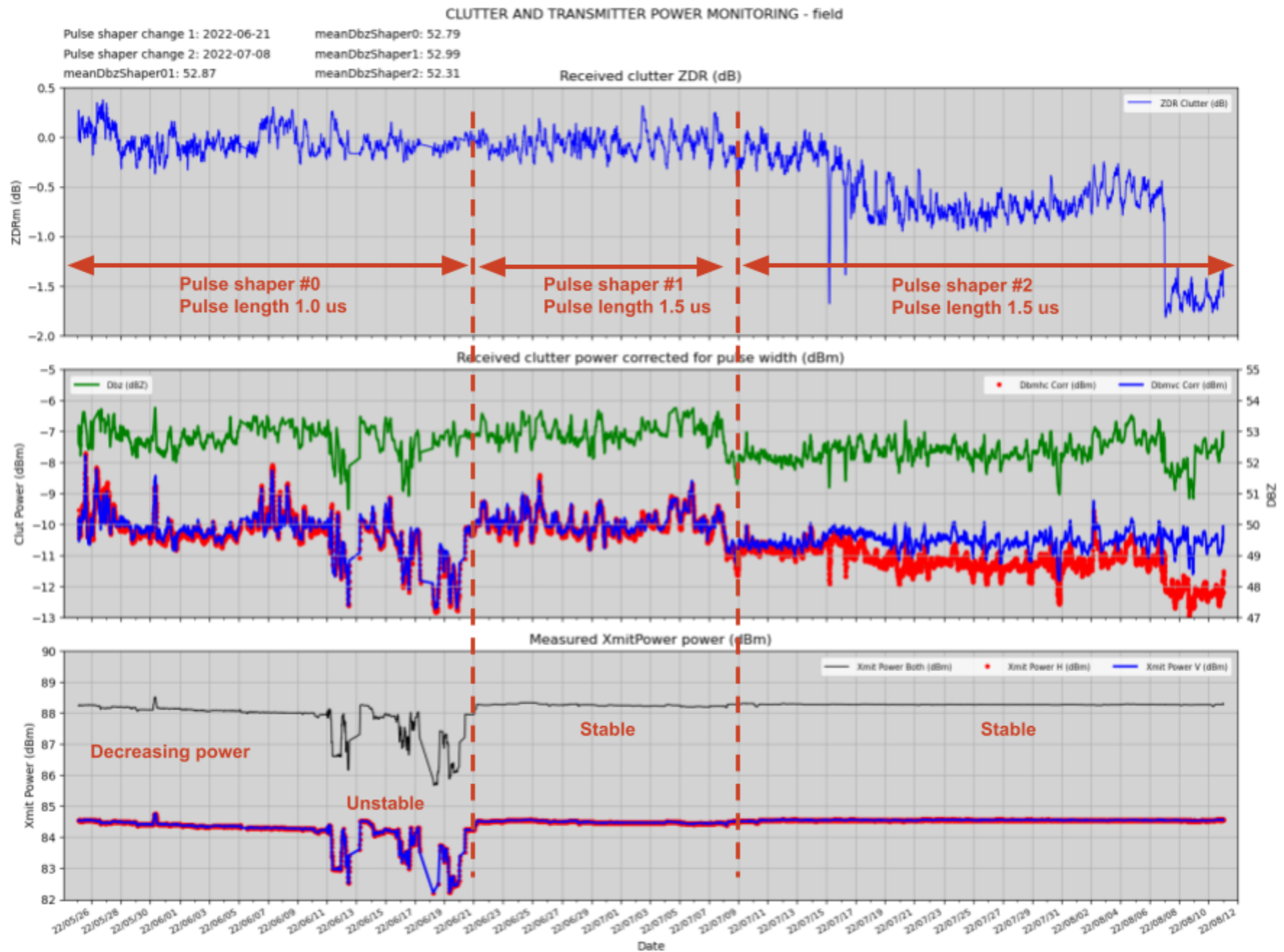


Figure 2.2: Clutter power and transmitter monitoring, during the field phase of the project.

2.2. Receiver calibration

The data plotted in Figure 2.2 suggests changes in the characteristics of both the transmitter and the receiver during the project.

In order to keep track of the receiver characteristics, we performed routine engineering calibrations for the receiver during the project, as operational time permitted.

The results from these calibrations can help to explain what occurred, particularly with the H channel receiver.

Figure 2.3 shows the calibration curves for the receiver during the time that pulse shaper #0 was in the system.

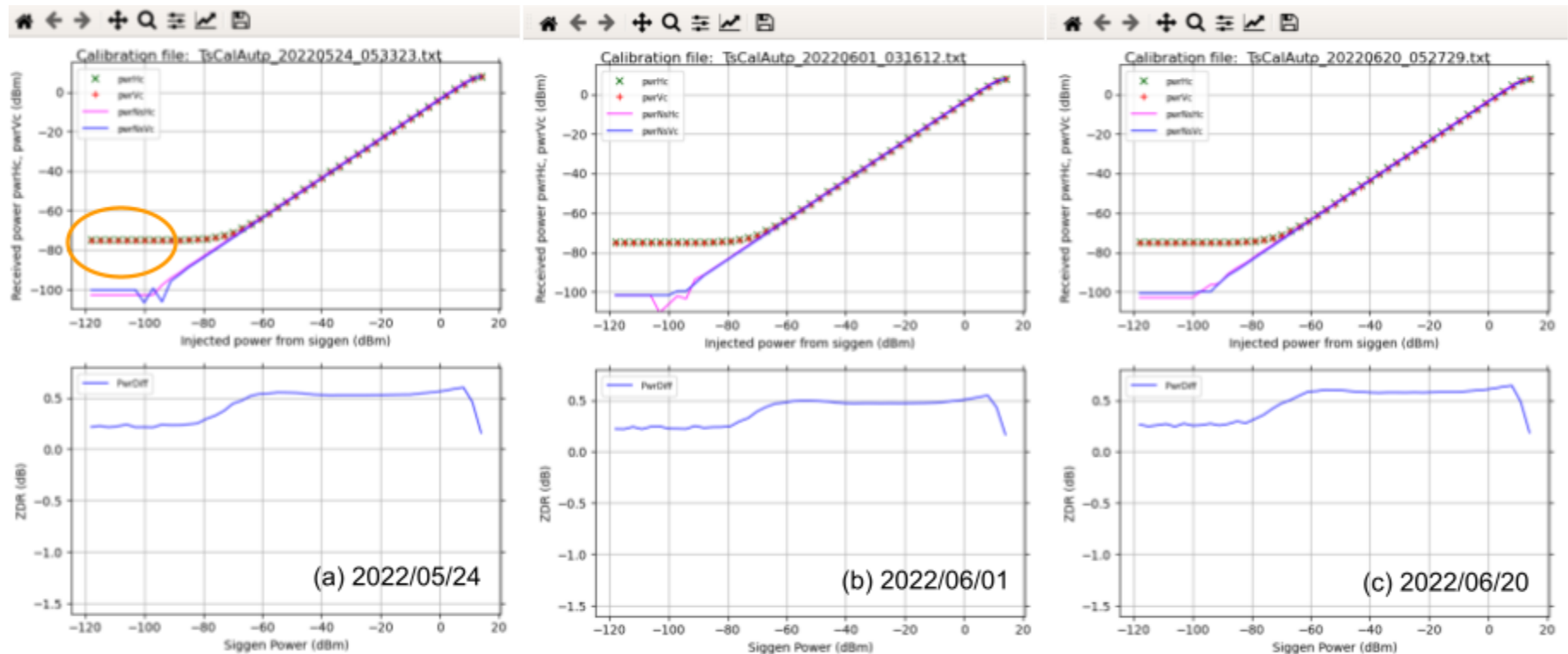


Figure 2.3: Calibrations 2022/05/24 to 2022/06/20.

The top panels show the measured power response (y axis) of the receiver to signals injected using a signal generator (x axis). The green crosses show the power values for the H channel, and the red plus signs for the V channel. The noise is computed using the values at the left of the plot - see the orange oval in (a) as an example. The magenta line shows the H power minus the H measured noise, and the blue line shows the V power minus the V measured noise.

The lower panels show the (H minus V) power difference - these are not corrected for noise.

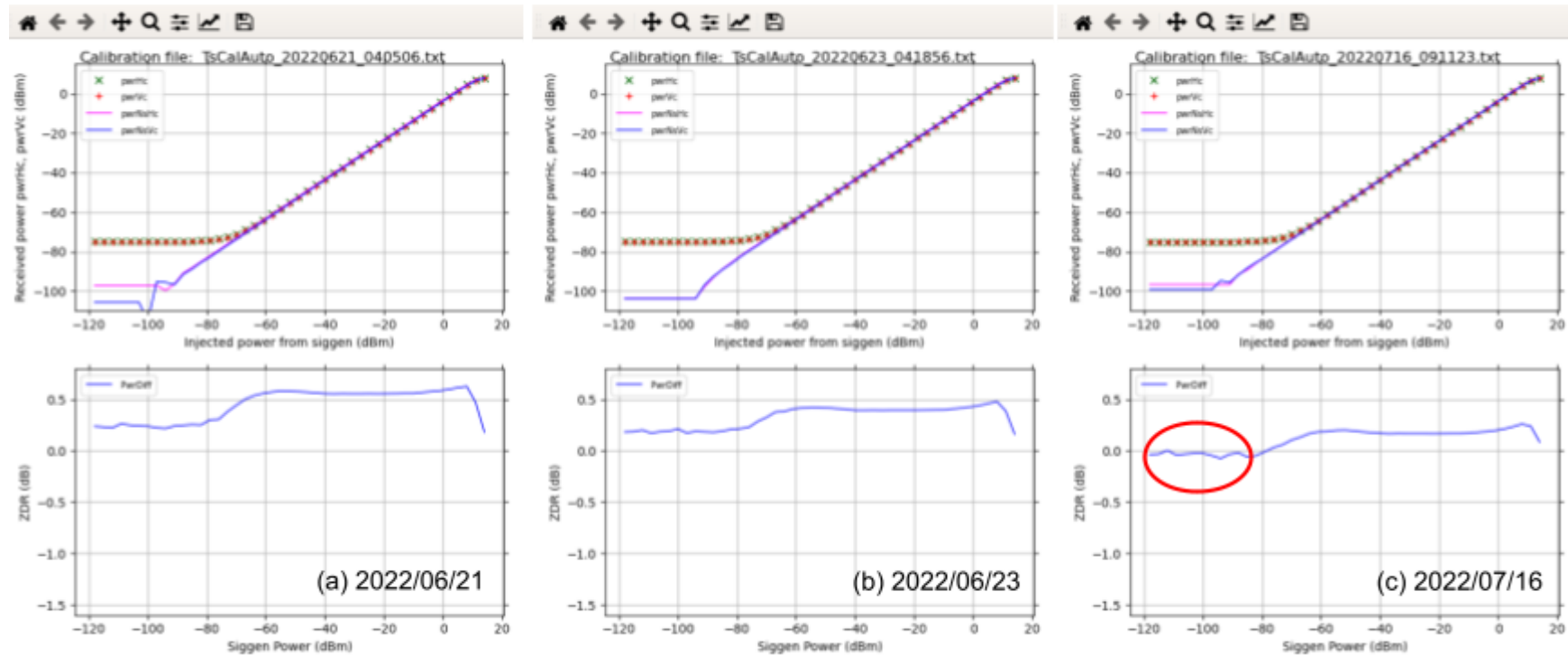


Figure 2.4: Calibrations from 2022/06/21 to 2022/07/16.

Figures 2.4 and 2.5 show the receiver calibration plots for the period after the original pulse shaper was replaced.

What these plots and Table 2.1 confirm is that the receiver characteristics remained quite stable from the start of the project at least until 2022/06/23. And the ZDR of the clutter presented in Figure 2.2 shows that this stability in the receiver continued until around 2022/07/15.

From 07/15 to 07/16 the ZDR of the clutter changed markedly (top panel, Figure 2.2). Figure 2.4 (c) shows the calibration on 2022/07/16. The lower panel of that figure shows that the (H minus V) received power difference has decreased by between 0.2 and 0.3 dB (red oval). This points to a decrease in the H channel receiver gain.

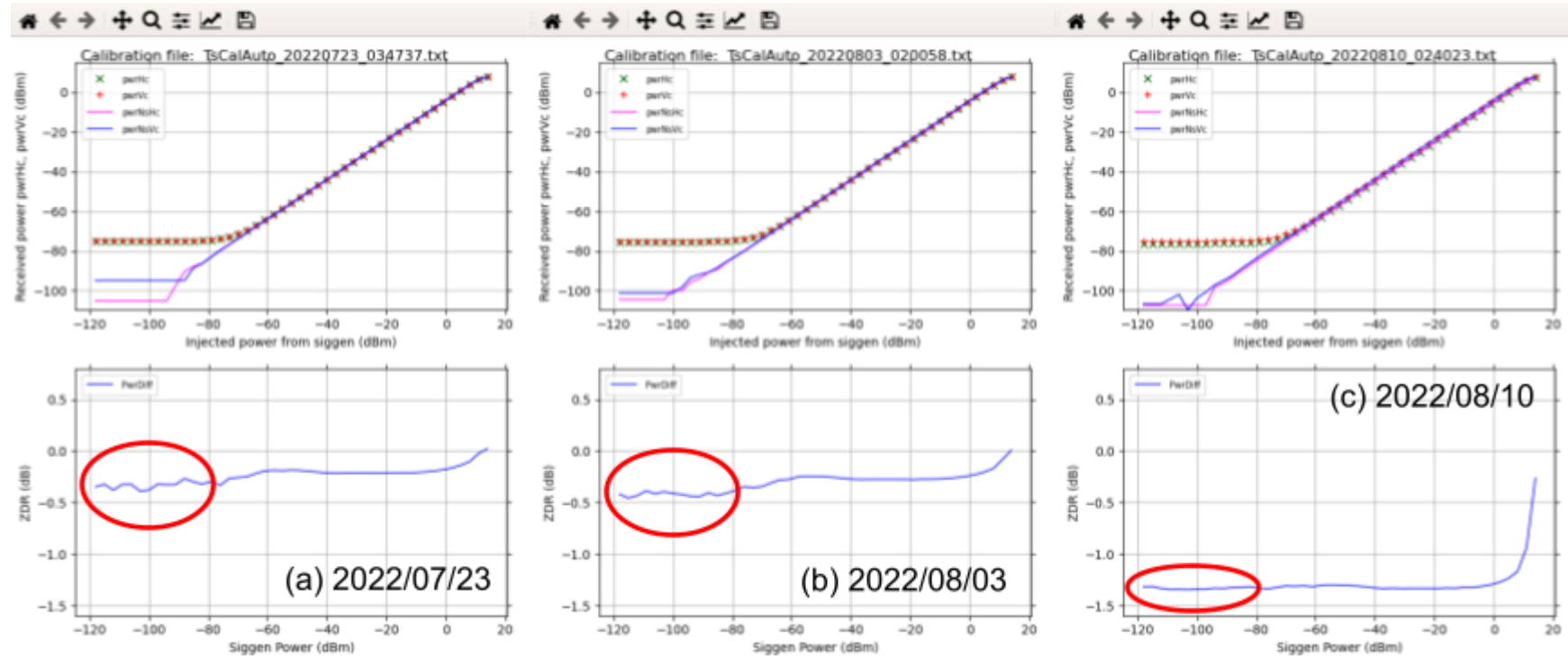


Figure 2.5: Calibrations from 2022/07/23 to 2022/08/10.

The calibration plots in Figure 2.5 show that this change in the H receiver gain continued - see red ovals. A large change occurred between 08/03 and 08/10. The top panel of Figure 2.2 shows that this change occurred around 08/08.

Table 2.1 below shows the noise values and receiver gains for each of the calibrations in Figures 2.3 through 2.5. The change in the H channel gain and noise is clear from 07/16 onwards. The V channel is stable throughout.

Table 2.1: Receiver measured noise and gain, for H and V channels, by date.

Date	Noise H channel	Noise V channel	Gain H channel	Gain V channel
2022/05/24	-74.89 dBm	-75.12 dBm	40.20 dB	39.46 dB
2022/06/01	-74.91 dBm	-75.14 dBm	40.16 dB	39.48 dB
2022/06/20	-74.88 dBm	-75.14 dBm	40.27 dB	39.48 dB
2022/06/21	-74.88 dBm	-75.12 dBm	40.27 dB	39.50 dB
2022/06/23	-74.88 dBm	-75.08 dBm	40.10 dB	39.49 dB

Date	Noise H channel	Noise V channel	Gain H channel	Gain V channel
2022/07/16	-75.12 dBm	-75.10 dBm	39.82 dB	39.44 dB
2022/07/23	-75.32 dBm	-74.97 dBm	39.44 dB	39.44 dB
2022/08/03	-75.58 dBm	-75.18 dBm	39.17 dB	39.23 dB
2022/08/10	-76.38 dBm	-75.05 dBm	38.36 dB	39.48 dB

2.3. Noise monitoring to estimate changes in receiver gain

In order to quantify the changes in receiver gain after 2022/07/15, we ran the NoiseMon application to estimate the noise from the time series data. The following parameters were used:

- averaging period: 12 minutes
- number of samples for moments computations: 128
- min elevation angle: 6 deg
- min height: 40 km
- min range: 100 km
- max range: 220 km (avoids the test pulse)
- min angular distance from the sun: 3 degrees
- max ray sum of echo at gates in excess of 35 dBZ: 250 dBZ
- min total number of gates for stats: 2000

The middle panel of Figure 2.6 below shows the noise for the H channel (red) and the V channel (blue). It clearly shows the changes in the H channel noise on 07/16 and 08/07. As discussed in section 3 above, this was caused by a change in the receiver gain in the H channel. The triangles show the receiver gains as computed from the engineering calibrations - i.e. the data in Table 2.1.

The top panel in Figure 2.6 shows the (H minus V) difference in noise values, plotted in black. The green dots on this panel show the measured ZDR bias from vertical pointing observations in rain. Figure 2.7 shows the dependence of the ZDR bias on temperature - this has been extensively documented in publications.

For the stable period from 05/25 to 07/09 the mean measured ZDR bias from vertical pointing was 0.75 dB, while the mean (H minus V) difference for the same period is 0.23 dB. The difference between these 2 quantities is 0.52 dB. If we adjust the black curve up by 0.52 dB we get the brown curve, which matches the mean measured ZDR bias. The orange curve is the brown curve adjusted for the temperature dependence shown in Figure 2.7.

As you can see from the top panel in Figure 6, the ZDR bias changes significantly from 07/16 onwards. In order to compute accurate Z and ZDR values for this part of the project we need to make use of the noise measurements to assess the changes in H channel receiver gain, and adjust the Z and ZDR moments for these changes in gain.

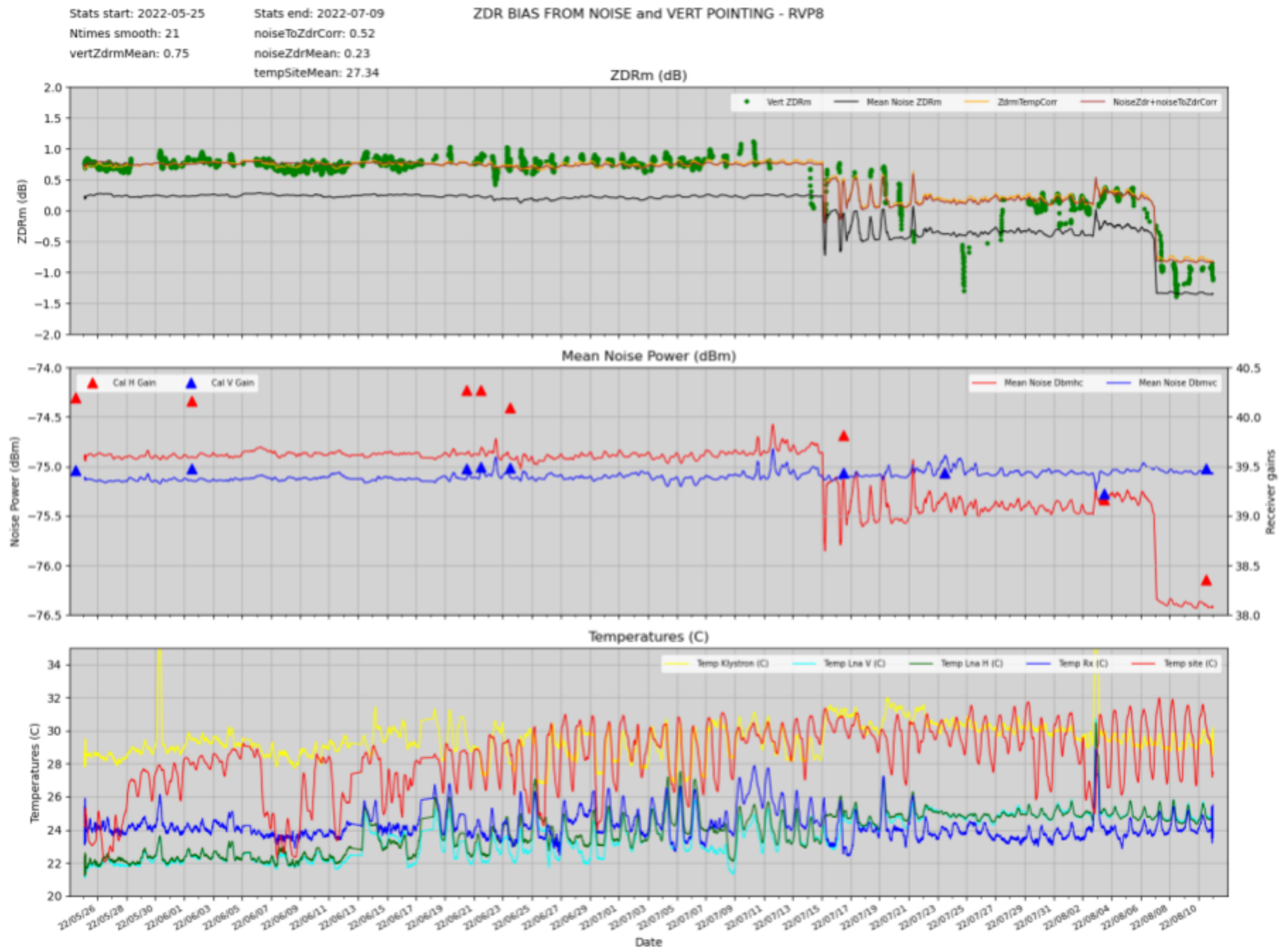


Figure 2.6: Noise power monitoring, combined with temperature monitoring and vertical pointing results for ZDR calibration.

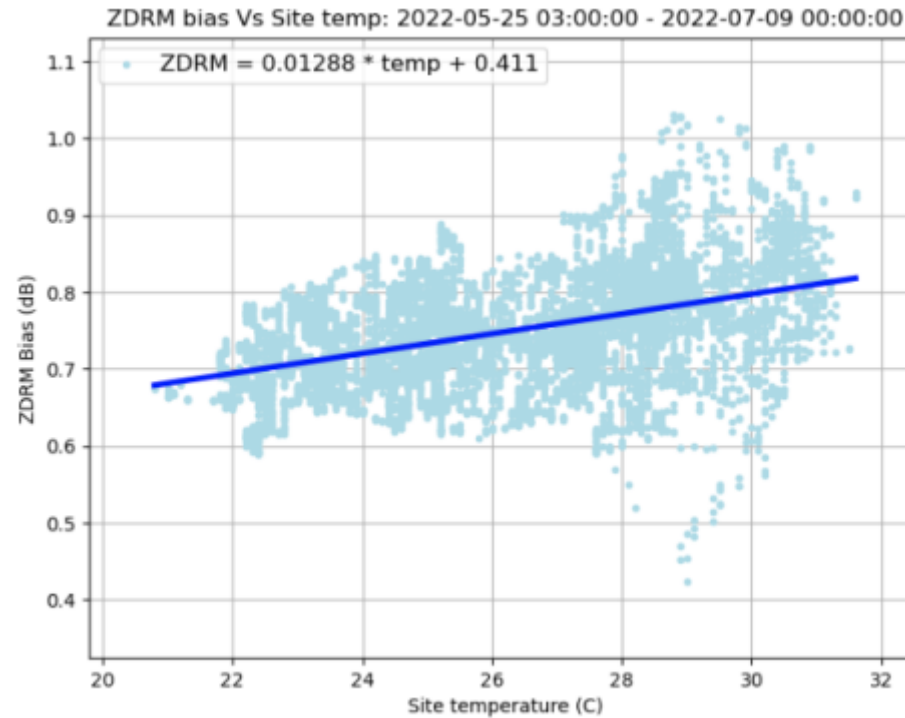


Figure 2.7: Measured ZDR bias, from vertical pointing, as a function of site temperature.

2.4. Monitoring using solar scans

Solar scans – sector box scans across the sun – were carried out at the start of the project, and routinely throughout the project, when possible.

These solar scans have 3 purposes:

1. To check the antenna angle alignment. The white cross shows the actual sun position, while the blue grid shows the ideal sun position.
2. To check the cross-correlation between the H and V channels.
3. To check the pattern of ZDR bias.
4. To check the absolute reflectivity calibration.

See Figures 2.8 and 2.9.

As can be seen from these figures, the antenna alignment was good – the alignment error remained below 0.04 degrees for the duration of the project.

The inner white circle is at 1 degree from the center, and the outer white circle at 2 degrees.

The ZDR pattern (Figure 2.8(c)) shows a gradient, especially outside the 1-degree circle. This is the result of a mismatch in the beam shape between the horizontal and vertical channels – see also Figure 2.9(c). The horizontal channel shape is quite circular, while the vertical channel shape is stretched in the vertical sense.

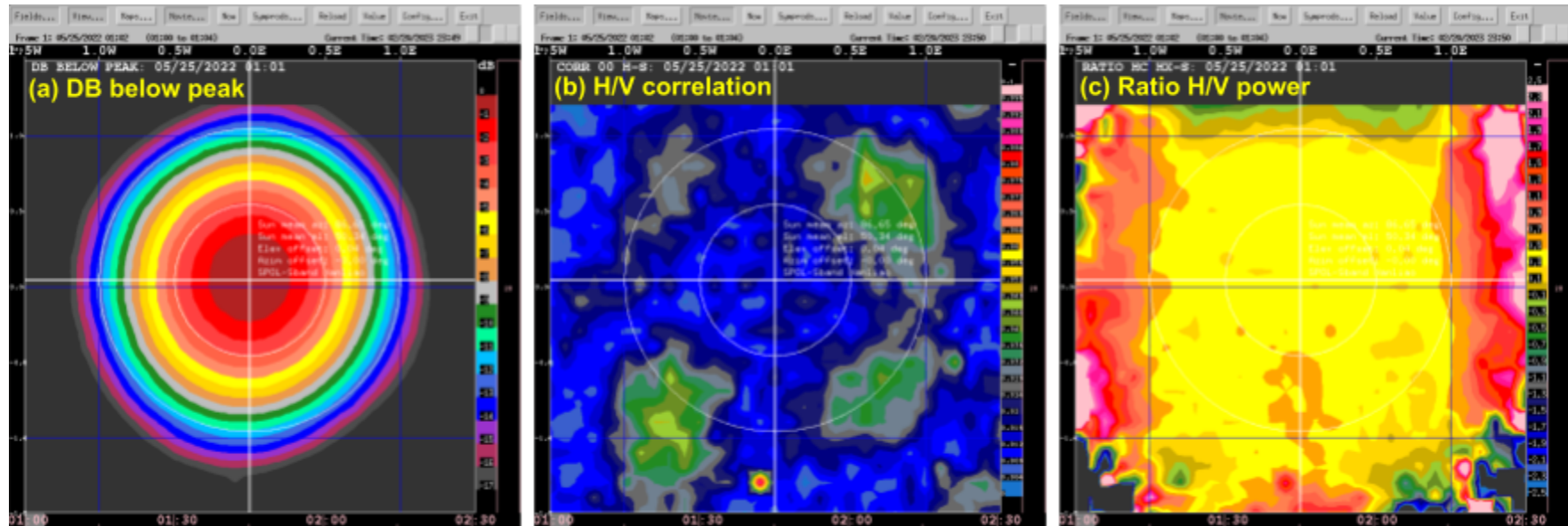


Figure 2.8: Results from example sun box scan, 2022/06/01 12:52 UTC.

Left: Power (dB) below solar peak power. Right: Ratio of V_c/H_c power (dB), i.e. solar ZDR pattern.

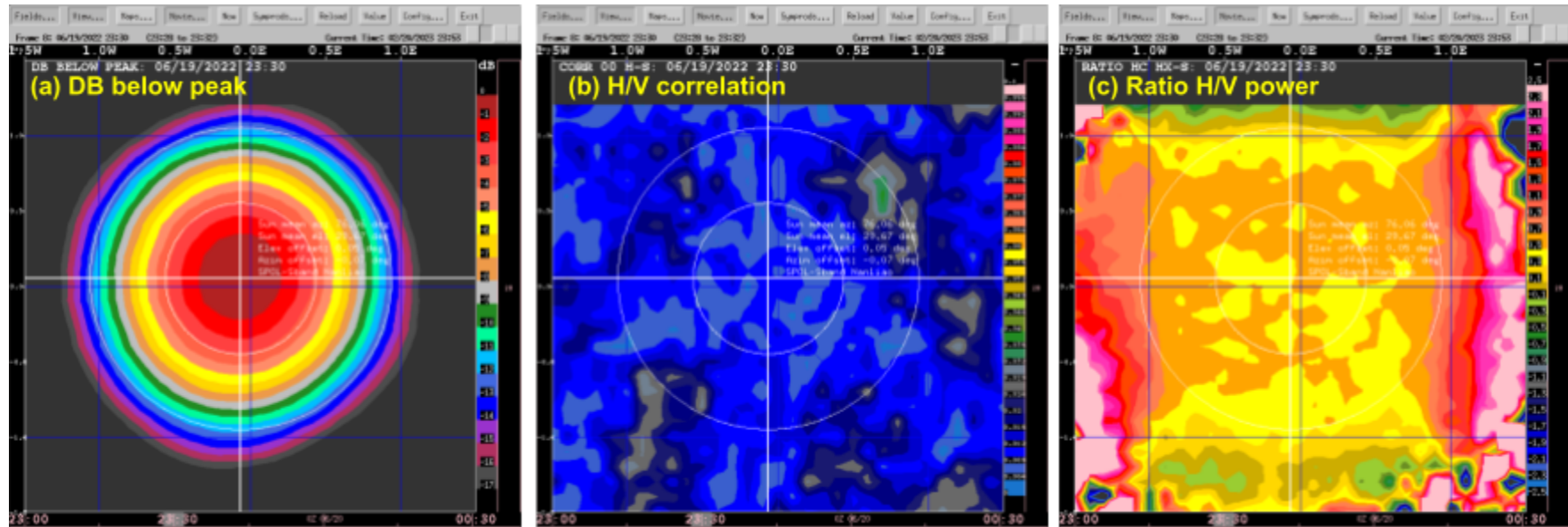


Figure 2.9: Sun box scan, 2022/06/01 12:52 UTC.

Left: Horizontal polarization co-polar power (dB). Right: Vertical polarization co-polar power (dB).

At the start of the project the radar was operated at the assigned frequency of 2840.0 MHz. Note that in Figure 2.8(b) the cross-correlation coefficient has patches that exceed 0.05. Ideally this should be 0. These patterns have correlation values that are considerably higher than those observed in Colorado when operating at our usual 2809 MHz frequency.

We postulated that the increased correlation values were the result of a change in beam pattern between H and V, perhaps related to the operating frequency. We performed a test at 2843 MHz, and the correlation pattern was much improved. However, we were not permitted to operate at that frequency. But we were allowed to use 2841.5 MHz, which is what we ultimately settled on for our operating frequency.

The correlation plot in Figure 2.9(b) shows the considerably lower correlation coefficients in the pattern. This was higher than normal, but better than Figure 2.8(b). The increased correlation may have contributed to apparently higher sidelobes than we normally observe.

We also monitored the power in the sun 'spikes' that are observed in the power data during routine scanning. Figure 2.10 shows the time series of the observed power in H and V from sun spikes (lower panel) and the ZDR values in the solar observations (H/V).

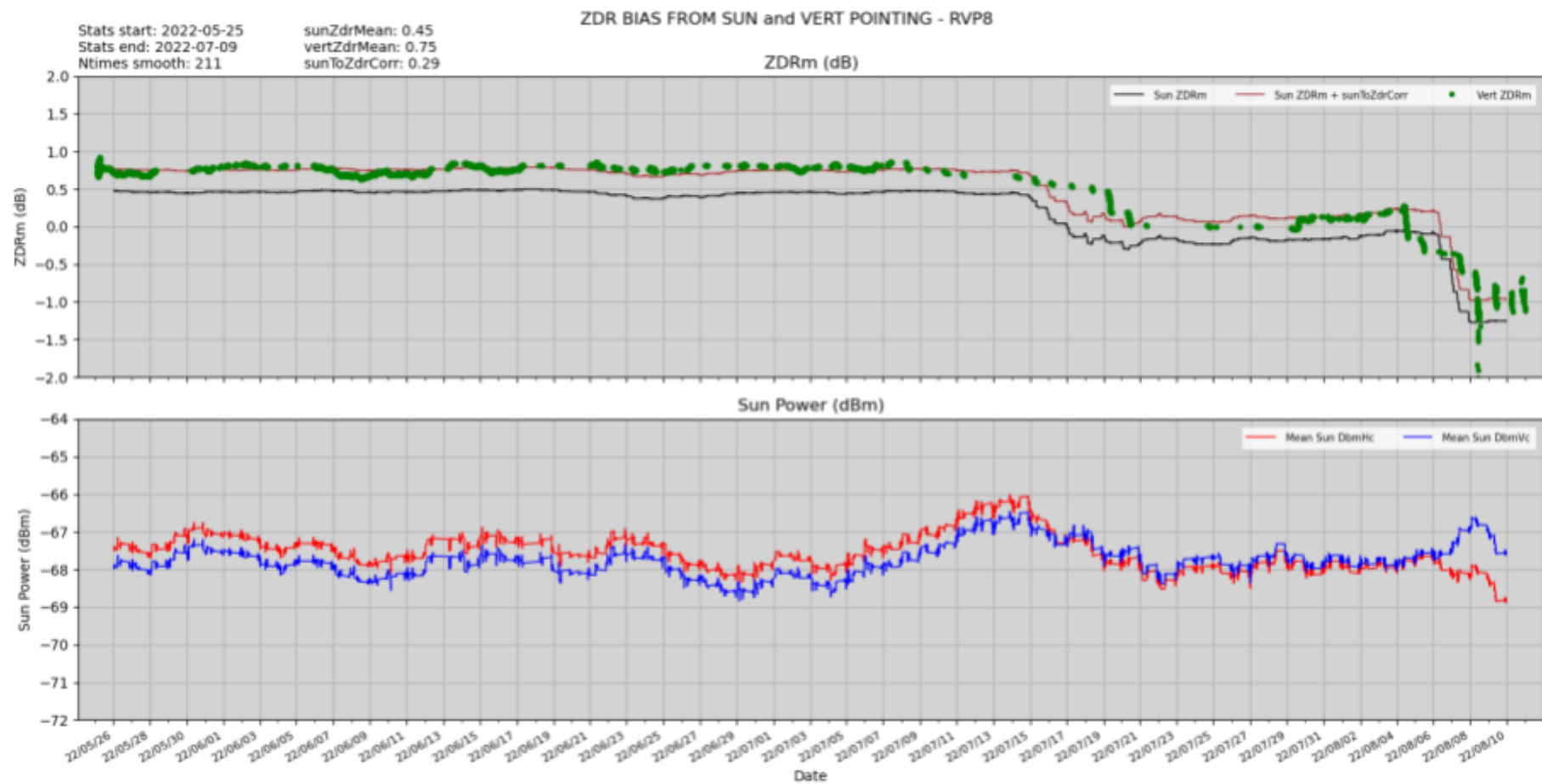


Figure 2.10: power in H and V channels observed from 'sun-spikes'.

3. Generating the QC1 data set

3.1 Generating the moments data from the time series

To generate the moments data set, we use 2 apps that communicate via a Fast Message Queue (FMQ):

- Iq2Dsr: reads the time series, computes the moments, and writes the moments to the FMQ.
- Dsr2Rads: reads the moments from the FMQ, creates surveillance and RHI volumes, and writes the data to CfRadial NetCDF files.

As shown in Figure 2.6, the changes in estimated noise for the H channel reflect the changes in gain from the periodic engineering calibrations. These corrections are stored in an SPDB database.

We can use the estimated noise values to correct the measured calibrations, and then apply these corrected values to the computations for Z and ZDR.

In addition, as we compute the moments we can censor the data based on NCP and SNR.

We censor a gate if **both** of the following conditions are met:

- $\text{SNR} < 0.0 \text{ dB}$
- $\text{NCP} < 0.2$

Even though some corrections are applied in this step, further corrections were required. Therefore we refer to this initial data set as 'partially-corrected' moments, as opposed to the 'field' moments.

3.2 Checking the partially-corrected moments data set.

After running Iq2Dsr and Dsr2Radx, the clutter monitoring step was performed again on the resulting partially-corrected data set.

Figure 3.1, below, shows the results of this process.

The green (DBZ) trace shows that the transmitter power instability has been corrected for.

However, after pulse shaper 2 was installed, the clutter power dropped by about 0.7 dB.

We also ran a further check on the ZDR calibration - see section 3.3.

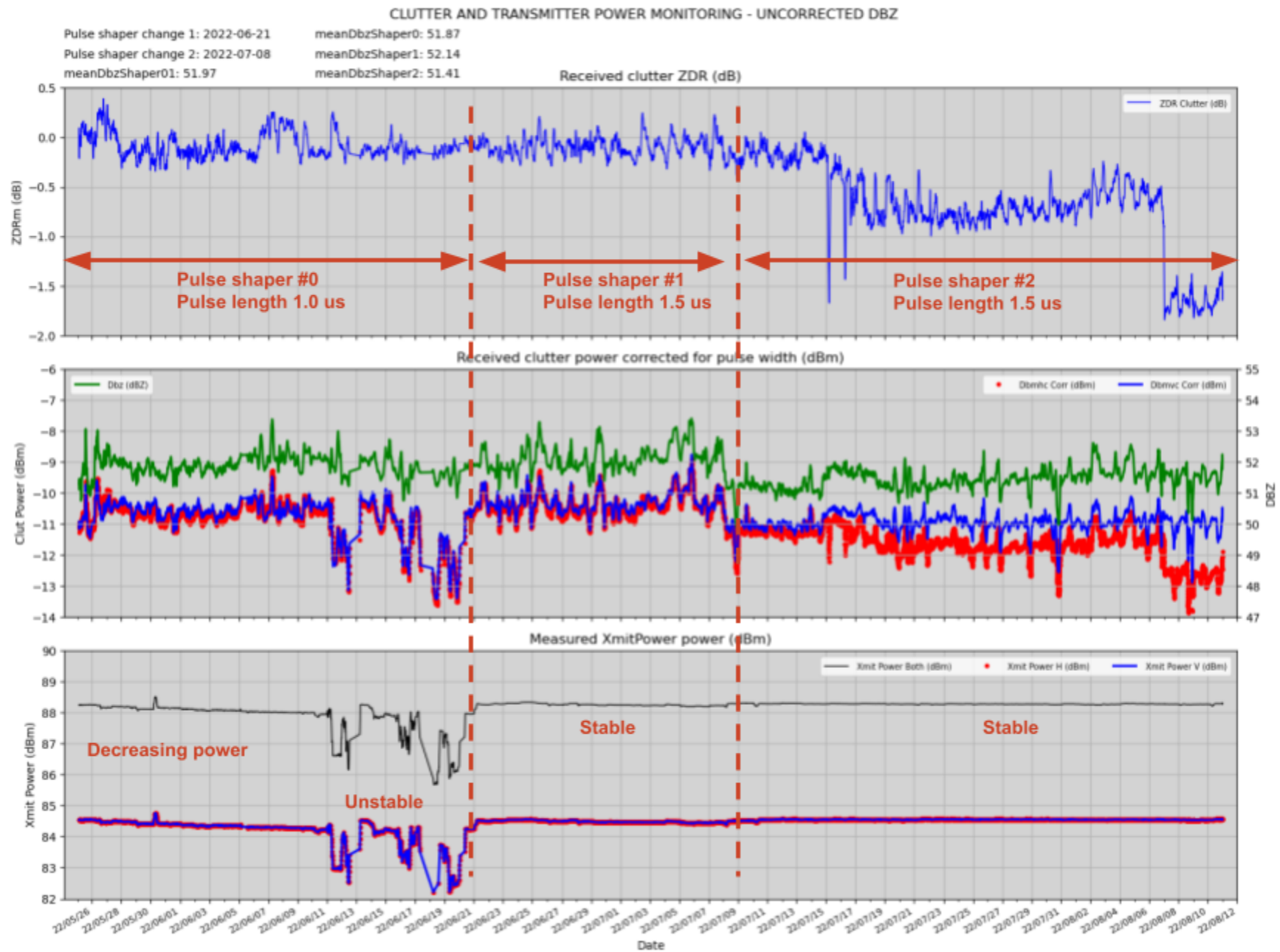


Figure 3.1: Clutter power and transmitter monitoring, partially corrected data set.

3.3 Checking the ZDR calibration using the Z vs ZDR relationship method

After all of the corrections made in the stages described above, we noticed that the ZDR values in regions of low reflectivity appeared to be biased low. For example Figure 3.2 shows the Z and ZDR fields for a warm rain case over the sea to the NW of the radar. The Z vs ZDR plot, plus the fit of the ZDR data, shows a median ZDR value of around 0 dB for reflectivity values of 20 dBZ. Published articles in the literature indicate that ZDR should typically be around 0.2 dB for reflectivity around 20 dBZ (Cocks et al., 2019, Gorgucci et al., 1999).

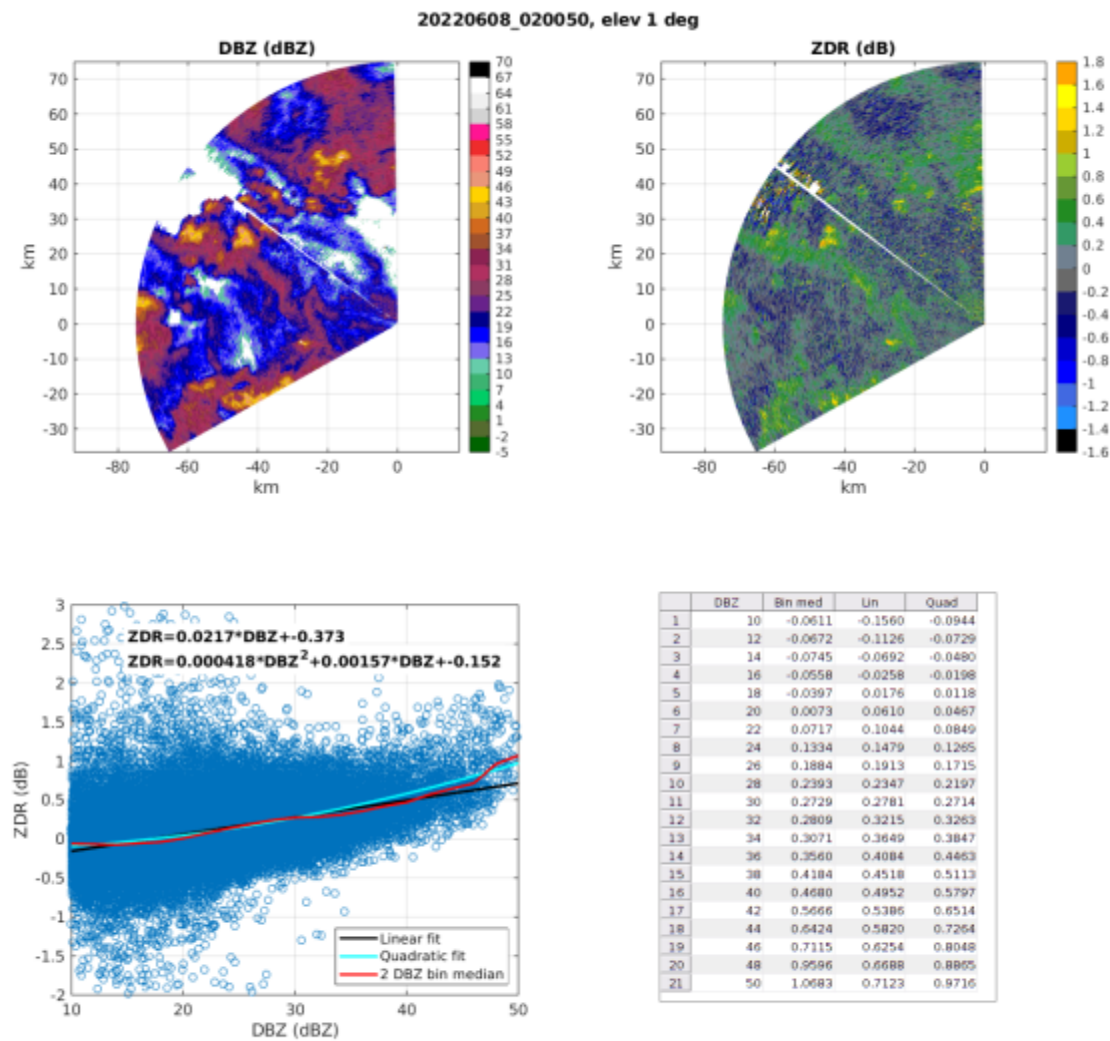


Figure 3.2: Example of Z vs. ZDR for warm rain to the NW of the radar.

We examined over 15 cases and came to the conclusion that the ZDR values were indeed low by about 0.2 dB. We corrected this by applying a 0.2 dB offset to all of the ZDR data for the project. And when we checked the results by generating plots for all of the 15 cases. Figure 3.3 shows the data from Figure 3.2 corrected by 0.2 dB.

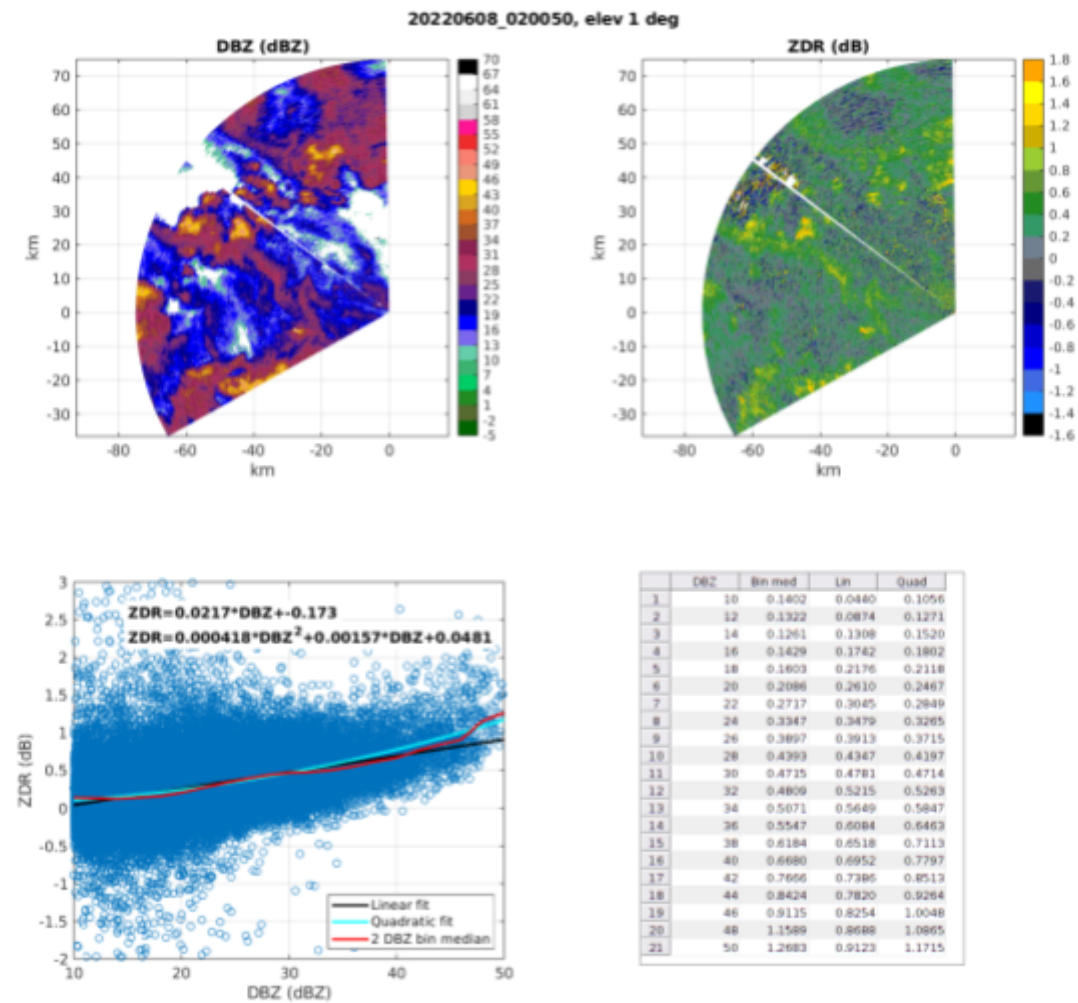


Figure 3.3: case from Figure 9, but corrected by applying an offset of +0.2 dB.

We therefore decided it was appropriate to increase the ZDR values by 0.2 dB throughout the project.

3.4. Applying further corrections to the moments data

It was also pointed out that the PHIDP values in the partially-corrected data set start out at highly positive values close to the radar. The problem with this is that PHIDP will then fold wherever a strong echo is encountered - in simultaneous mode PHIDP ranges from -180 and +180 degrees. In order to limit folding, the PHIDP values need to be systematically increased so as to be close to -170 deg close to the radar. That provides room for PHIDP to increase through echo without folding.

Based on the above discussions we made the following corrections to the partially-corrected data set:

- increased DBZ by 0.7 dB from 2022/07/09 onwards.
- increased ZDR by 0.2 dB everywhere.
- added 40 degrees to PHIDP everywhere.

We ran RadxConvert to apply these corrections. The result is the 'corrected' moments data set.

3.5. Checking the corrected data set

We once again re-ran the clutter monitoring process to ensure that the corrections were applied satisfactorily.

Figure 3.4 shows the results. As you can see from the green trace in the middle panel, the gain changes have been accounted for and the mean reflectivity from clutter is now reasonably constant for the duration of the project. Also the change in pulse width associated with pulse shaper #2 has been corrected for.

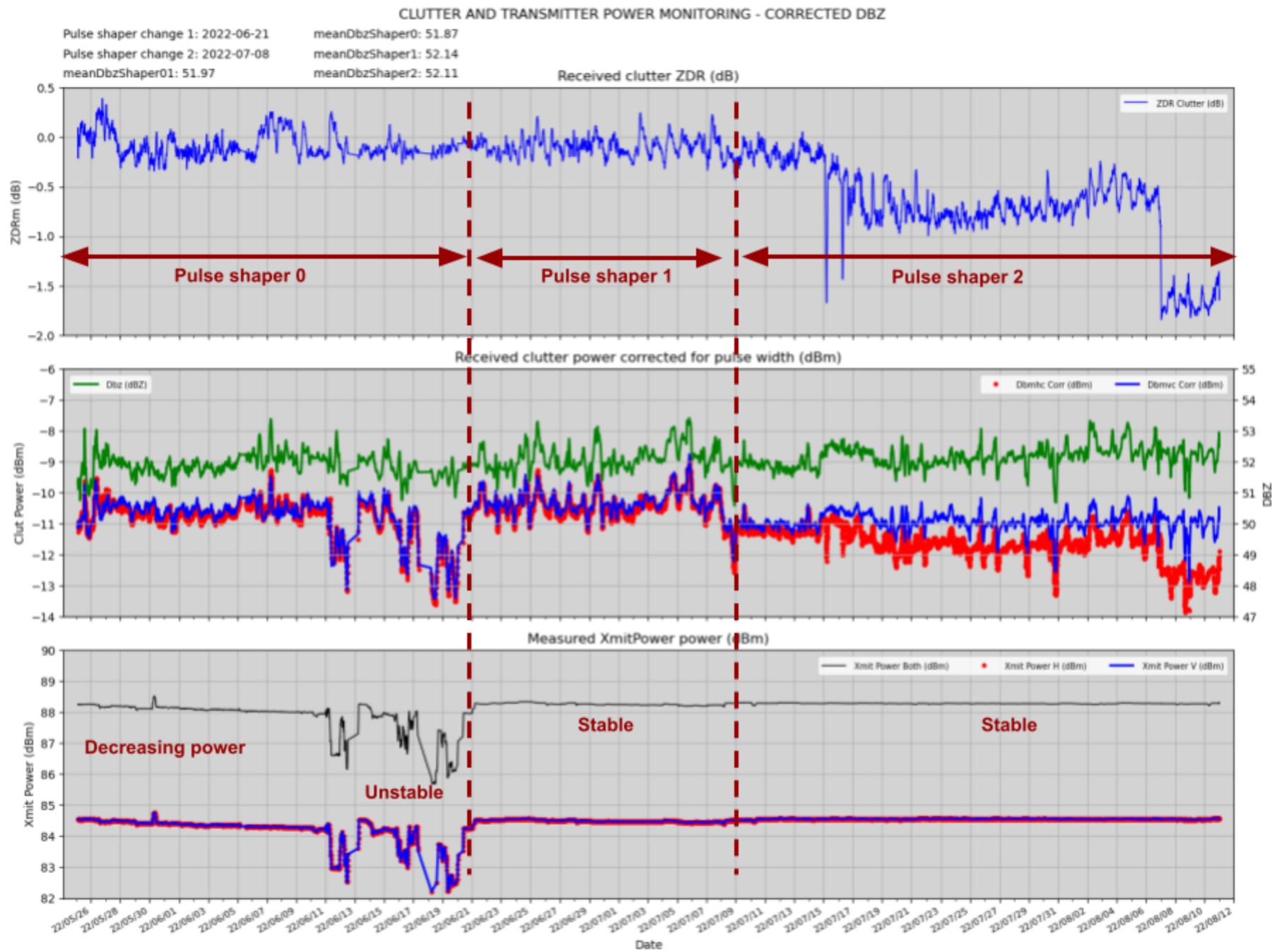


Figure 3.4: results of clutter monitoring analysis, for the corrected moments.

4. Creating the derived fields - Particle ID (PID) and precipitation rate (QC1, Version 1.0)

4.1 Running RadxRate

After the moments data had been corrected (section 3) we ran the application RadxRate to create the PID and precipitation rate fields.

4.2. Missing data in RHIs at 101/281 degrees

One of the scan strategies for the S-Pol scan at PRECIP was to collect RHIs lined up with SEAPOL on Yonaguni. These RHIs, at azimuth angles of 101 and 281 degrees, worked fine in real-time mode.

However, when we reprocessed the time series data we found missing data in these RHIs. This revealed a bug in our time series archiving software. Because our scan sequence operated on a 12-minute schedule, the antenna would often stop and wait at the start of the 101-degree RHI. Our software was set up to stop saving time series when the antenna stopped. When the antenna started moving again it took a couple of seconds to restart the time series recording. Therefore we lost some of the data in the 101-degree RHI.

To overcome this problem, we decided to use the moments data from the field RHIs, and correct them for all of the procedures carried out above. We performed this in a number of steps:

1. analyze the difference between the Z and ZDR fields in surveillance field volumes and QC1 volumes;
2. store those differences in SPDB files, indexed by time;
3. apply those differences to correct the field versions of the 101-degree and 281 degree RHIs.

This procedure was carried out by running the FixFieldVals application twice, first to perform the analysis in steps 1 and 2 above, and second to perform step 3.

Figure 4.1 shows the offsets that were estimated by running FixFieldVals in analysis mode, using surveillance data.

We then ran FixFieldVals to apply these offsets to the field RHIs that were collected using the PrecipRhi1 scan - these being the RHIs at azimuths of 101 and 281 deg.

The corrected RHIs were then manually merged into the v1.0 data set, using rsync.

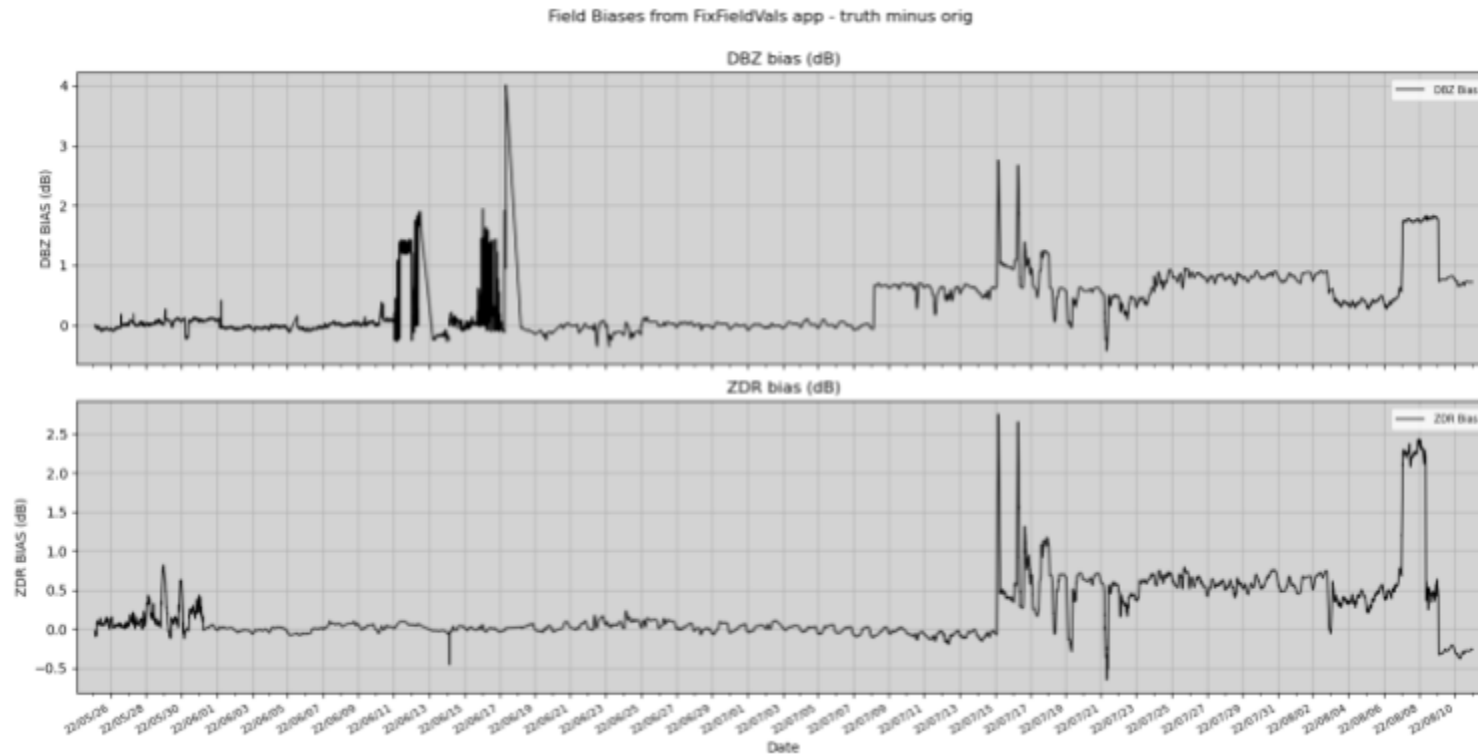


Figure 4.1: time series of the differences in the Z and ZDR fields, comparing the field surveillance volumes to the QC1 volumes.

4.3. Creating quick-look images to check the full data set

In order to quickly look through the final data set, to check for errors etc., we created quick-look images using the CIDD display app.

Figure 4.2 shows the gwenview application displaying the quick-look images.

We also created movie-loops for each field, for each day, also for quickly checking for data quality.

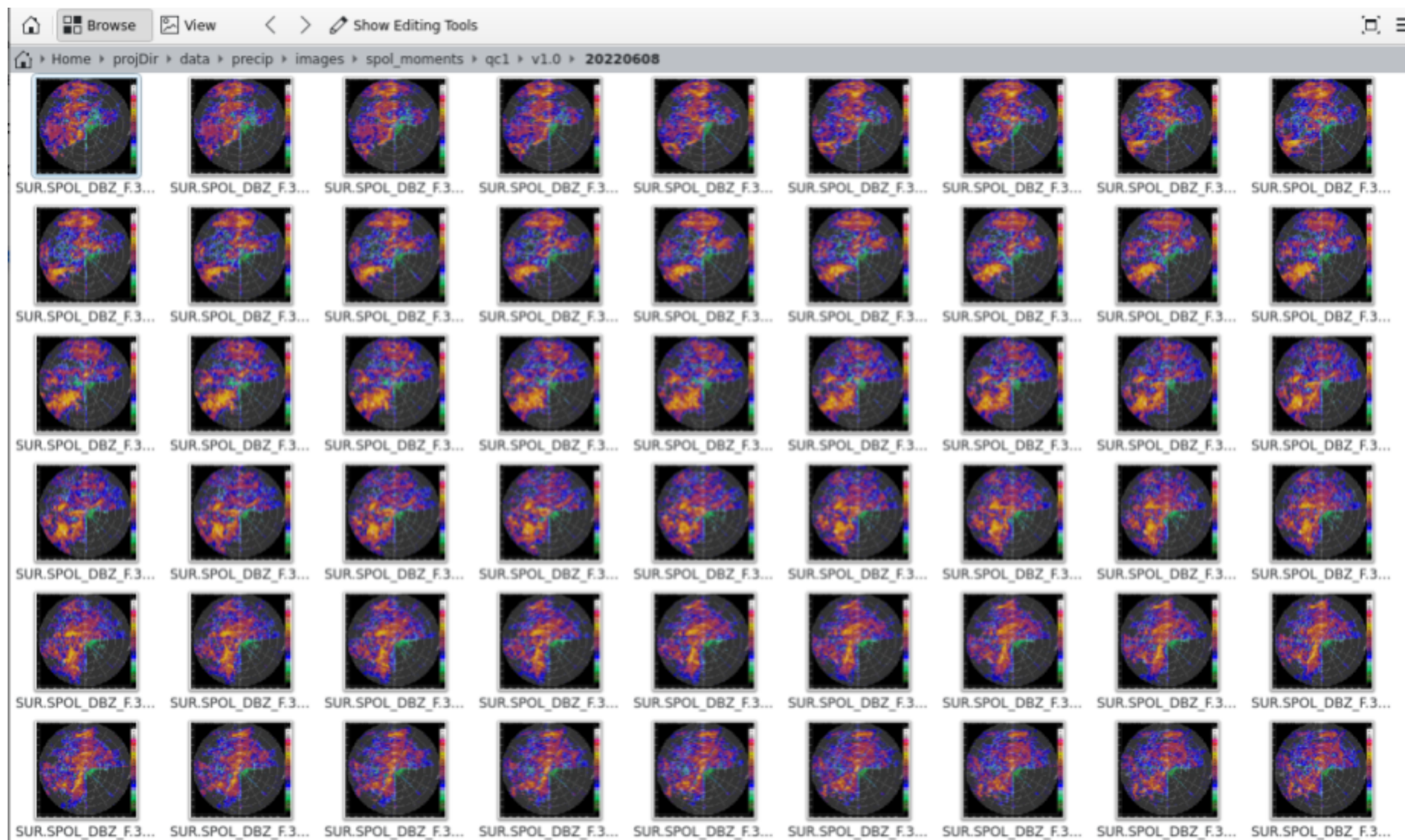


Figure 4.2: gwenview displaying quick-look images (in this case for DBZ) to check the final data set.

After reviewing the quick-look images and movie loops, incomplete scans, or scans with bad data, were removed from the data set. This was done manually.

The result is the Version 1.0 data set.

5. Fields in the QC data set CfRadial files

The following is a list of the parameters included in the quality-controlled, CfRadial format, S-Pol data set. This applies to the data set released on 2023/02/28 (Version 1.0). Comments and references are shown, as appropriate. Please refer to the CfRadial format description for further information (Dixon, et al., 2016).

Parameters have had noise correction and/or censoring applied, as appropriate. Note that noise correction is dependent upon noise analysis as described in section 2.3.

Clutter-filtered fields are indicated with **_F**.

Table 5.1: list of fields in QC1/v1.0 data set.

Parameter Units	Standard Name Long Name	Comments:
DBZ dBZ	equivalent_reflectivity_factor radar_reflectivity	Unfiltered, calibrated and corrected; elevation angle-dependent atmospheric attenuation applied, as in Doviak and Zrnice, 1993 (pp.44-45).
DBZ_F dBZ	equivalent_reflectivity_factor radar_reflectivity	Clutter filtered, calibrated and corrected; elevation angle-dependent atmospheric attenuation applied, as in Doviak and Zrnice, 1993 (pp.44-45).
VEL m/s	radial_velocity_away_from_instrument radial_velocity_unfolded_using_vel_hv	Unfiltered, traditional fast-alternating dual-pol velocity estimate, from H and V interspersed signal, with phase offset (Wilson/Illingworth/Blackman, 1997). This velocity is noisy if PHIDP is noisy. Nyquist velocity is ~26.7 m/s.
VEL_F m/s	radial_velocity_away_from_instrument radial_velocity_unfolded_using_vel_hv	Clutter filtered, traditional fast-alternating dual-pol velocity estimate, from H and V interspersed signal, with phase offset (Wilson/Illingworth/Blackman, 1997). This velocity is noisy if PHIDP is noisy. Nyquist velocity is ~26.7 m/s.
WIDTH m/s	doppler_spectrum_width doppler_spectrum_width	Unfiltered, Doppler spectrum width.
WIDTH_F m/s	doppler_spectrum_width doppler_spectrum_width	Clutter filtered, Doppler spectrum width.
NCP	normalized_coherent_power normalized_coherent_power	Unfiltered. lag1 power / lag0 power. Also known as SQI (signal quality index).
NCP_F	normalized_coherent_power normalized_coherent_power	Clutter filtered. lag1 power / lag0 power. Also known as SQI (signal quality index).
ZDR_F dB	log_differential_reflectivity calibrated_log_differential_reflectivity	Clutter filtered, ZDR, calibrated. Defined by Seliga and Bringi, 1976. Derived from calibrated copolar reflectivities; corrected through use of various techniques, as detailed elsewhere in this report.
PHIDP_F deg	differential_phase_hv differential_phase	Clutter filtered. See Jameson and Mueller, 1985; processed according to Hubbert and Bringi, 1995.

KDP_F deg/km	specific_differential_phase_hv specific_differential_phase	Clutter filtered. Processed by NCAR filtering technique. Corrected using Z/ZDR method.
RHOHV_F	cross_correlation_ratio_hv cross_correlation_ratio	Noise-corrected RHOHV. Provides a more consistent value in regions of low SNR. Reprocessed from original (in-field) covariance data set. (See Zrnic, 1988 for formulation).
RHOHV_NNC_F	cross_correlation_ratio_hv cross_correlation_ratio_not_noise_corrected	Original, in-field RHOHV, not noise corrected.
SNRHC dB	signal_to_noise_ratio_hc signal_to_noise_ratio_db_h_copol_channel	Unfiltered. Noise correction applied.
SNRHC_F dB	signal_to_noise_ratio_hc signal_to_noise_ratio_db_h_copol_channel	Clutter filtered. Noise correction applied.
SNRVC dB	signal_to_noise_ratio_vc signal_to_noise_ratio_db_v_copol_channel	Unfiltered. Noise correction applied.
SNRVC_F dB	signal_to_noise_ratio_vc signal_to_noise_ratio_db_v_copol_channel	Clutter filtered. Noise correction applied.
DBMHC dBm	log_power_hc power_in_dbm_h_copol_channel	Unfiltered. No noise correction applied.
DBMHC_F dBm	log_power_hc power_in_dbm_h_copol_channel	Clutter filtered. No noise correction applied.
DBMVC dBm	log_power_vc power_in_dbm_v_copol_channel	Unfiltered. No noise correction applied.
DBMVC_F dBm	log_power_vc power_in_dbm_v_copol_channel	Clutter filtered. No noise correction applied.
CMD_FLAG none	clutter_mitigation_decision_flag clutter_mitigation_interest_flag	1 if clutter filter applied at this gate 0 if clutter filter not applied at this gate See Steiner and Smith, 2002; Hubbert, <i>et al.</i> , 2009a, and Hubbert, <i>et al.</i> , 2009b.
PID	hydrometeor_type particle_id	See Vivekanandan, <i>et al.</i> , 1999 for details. Modifications made by Scott Ellis for PECAN. The in-field version of PID differs slightly from the final PID.
TEMP_FOR_PID C	temperature temperature_for_computing_pid	Temperature from nearest-in-time, nearest-in-space sounding information.
RATE_ZH mm/hr	precip_rate_from_z precip_rate_from_z	Precip rate from Z.
RATE_HYBRID mm/hr	precip_rate_hybrid_of_zh_zzdr_kdp_and_kdpzdr precip_rate_hybrid_of_zh_zzdr_kdp_and_kdpzdr	NCAR hybrid precip rate.

6. Procedures followed to create the data set (NCAR internal)

The parameter files for the QC are in:

`~/projDir/qc/params`

The scripts for running the QC are in:

`~/projDir/qc/scripts`

The top-level data directory on the cirrus server is:

`/scr/cirrus3/rsfdata/projects/precip`

Table 6.1: list of applications used in QC analysis.

Script name	Param file(s)	Input dir(s)	Output dir	Comments	Section
run_RadxClutter.sband	Rad Clutter.band	grids/spol/radarPolar/field/moments/sband/sur	grids/spol/radarPolar/clutter/sband/sur	Read field moments data, identify gates at which clutter is persistent, store clutter stats.	2.1
run_HawkEye.clutter.sband	HawkEye.clutter.sband			Display clutter stats. See Figure 2.1.	2.1
run_RadxClutMon.sband.field	RadxClutMon.sband.field	grids/spol/radarPolar/clutter/sband/sur grids/spol/radarPolar/field/moments/sband/sur	calibration/spol/clut_mon/field/sband/spdb	Compute power, SNR, Z and ZDR for clutter targets, using the field data. This allows us to monitor the changes in clutter returns over time.	2.1
run_SpdxXml2Table.clut_mon.sband.field	SpdxXml2Table.clut_mon.sband.field	calibration/spol/clut_mon/field/sband/spdb	calibration/spol/clut_mon/field/sband/tables	Convert SPDB data to a comma-delimited ASCII table.	2.1
run_PlotClutMon.sband.field		calibration/spol/clut_mon/field/sband/tables		Plot clutter stats and power monitoring data from the field, using the comma-delimited ASCII table. See Figure 2.2.	2.1
CalPlotQc.py e.g. run as follows: CalPlotQc.py --file ~/projDir/calibration/results/cal.sband.1.0us.sim/Ts CalAuto_20220620_052729.txt		~/projDir/calibration/results/cal.sband.1.0us.sim ~/projDir/calibration/results/cal.sband.1.5us.sim		See Figures 2.3, 2.4 and 2.5.	2.2
run_NoiseMon.sband	NoiseMon.sband	time_series/sband/save	calibration/spol/noise_mon/sband/spdb	Read through the time series, computing the mean measured noise for every 12 minute volume. Store the results in Spdb.	2.3

Script name	Param file(s)	Input dir(s)	Output dir	Comments	Section
run_SpdxXml2Table.noise_mon.sband	SpdxXml2Table.noise_mon.sband	calibration/spol/noise_mon/field/sband/spdb	calibration/spol/noise_mon/field/sband/tables	Convert SPDB data to a comma-delimited ASCII table.	2.3
run_PlotNoiseMon.sband	calibration/spol/noise_mon/field/sband/tables			Plot results of noise monitoring using comma-delimited ASCII table. See Figures 2.6 and 2.7.	2.3
run_RadxSunMon.sband	RadxSunMon.sband	grids/spol/radarPolar/field/moments/sband	calibration/spol/sun_mon/sband/spdb	Run analysis to find sun spikes in the SUR and RHI data. Estimate the powers for each channel. Save results in SPDB.	2.4
run_SpdxXml2Table.sun_mon.sband	SpdxXml2Table.sun_mon.sband	calibration/spol/sun_mon/sband/spdb	calibration/spol/sun_mon/sband/tables	Convert SPDB data to a comma-delimited ASCII table.	2.4
run_PlotSunMon.sband		calibration/spol/sun_mon/sband/tables		Plot results of sun monitoring using comma-delimited ASCII table. See Figure 2.10	2.4
run_Dsr2Radx.qc.sband.group1	Dsr2Radx.qc.sband	\$MOMENTS_FMQ_PATH	grids/spol/radarPolar/qc1/moments/sband/uncorrected	Runs 4 instances of Dsr2Radx to read moments results from Iq2Dsr. Start this first, before Iq2Dsr. This saves out the computed moments fields to CfRadial files.	3.1
run_Iq2Dsr.qc.sband.group1	Iq2Dsr.qc.sband	time_series/sband/save	\$MOMENTS_FMQ_PATH	Runs 4 instances of Iq2Dsr, to compute moments and feed the data to Dsr2Radx.group1 instances. Start this after run_Dsr2Radx.group1. Processes data from 2022/06/25 to 2022/07/03. This computes the moments, adjusting the calibration for the noise values estimated by NoiseMon. It also censors the gates based on SNR and NCP.	3.1
run_Dsr2Radx.qc.sband.group2	Dsr2Radx.qc.sband	\$MOMENTS_FMQ_PATH	grids/spol/radarPolar/qc1/moments/sband/uncorrected	Runs 4 instances of Dsr2Radx to read moments results from Iq2Dsr. Start this first, before Iq2Dsr. This saves out the computed moments fields to CfRadial files.	3.1
run_Iq2Dsr.qc.sband.group2	Iq2Dsr.qc.sband	time_series/sband/save	\$MOMENTS_FMQ_PATH	Runs 4 instances of Iq2Dsr, to compute moments and feed the data to Dsr2Radx.group2 instances. Start this after run_Dsr2Radx.group1. Processes data from 2022/07/03 to 2022/08/11. This computes the moments, adjusting the calibration for the noise values estimated by NoiseMon. It also censors the gates based on SNR and NCP.	3.1
run_RadxClutMon.sband.uncorrected	RadxClutMon.sband.uncorrected	grids/spol/radarPolar/clutter/sband/sur	calibration/spol/clut_mon/qc1/uncorrected/sband/spdb	Compute power, SNR, Z and ZDR for clutter targets, using the field data. This	3.2

Script name	Param file(s)	Input dir(s)	Output dir	Comments	Section
		grids/spol/radarPolar/qc1/moments/sband/uncorrected/sur		allows us to monitor the changes in clutter returns over time.	
run_SpdxXml2Table.clut_mon.sband.uncorrected	SpdxXml2Table.clut_mon.sband.uncorrected	calibration/spol/clut_mon/qc1/uncorrected/sband/spdb	calibration/spol/clut_mon/qc1/uncorrected/sband/tables	Convert SPDB data to a comma-delimited ASCII table.	3.2
run_PlotClutMon.sband.uncorrected		calibration/spol/clut_mon/qc1/uncorrected/sband/tables		Plot clutter stats and power monitoring data from the partially-corrected data set, using the comma-delimited ASCII table. See Figure 3.1.	3.2
~/projDir/qc/dataCheck/dbzVSzdr.m				Use Matlab script to analyze Z vs ZDR. See figures 3.2 and 3.3.	3.3
run_RadxConvert.apply_corrections	RadxConvert.apply_corrections	grids/spol/radarPolar/qc1/moments/sband/uncorrected	grids/spol/radarPolar/qc1/moments/sband/corrected	Apply DBZ, ZDR and PHIDP corrections to the uncorrected moments data. Writes out CfRadial files with corrected moments.	3.4
run_RadxClutMon.sband.corrected	RadxClutMon.sband.corrected	grids/spol/radarPolar/clutter/sband/sur grids/spol/radarPolar/qc1/moments/sband/corrected/sur	calibration/spol/clut_mon/qc1/corrected/sband/spdb	Compute power, SNR, Z and ZDR for clutter targets, using the corrected data. This allows us to monitor the changes in clutter returns over time.	3.5
run_SpdxXml2Table.clut_mon.sband.corrected	SpdxXml2Table.clut_mon.sband.corrected	calibration/spol/clut_mon/qc1/corrected/sband/spdb	calibration/spol/clut_mon/qc1/corrected/sband/tables	Convert SPDB data to a comma-delimited ASCII table.	3.5
run_PlotClutMon.sband.field		calibration/spol/clut_mon/qc1/corrected/sband/tables		Plot clutter stats and power monitoring data from the field, using a comma-delimited ASCII table. See Figure 3.4.	3.5
run_RadxRate.qc	RadxRate.qc pid_params.spol.sim pid_thresholds.spol.sim rate_params.spol	features/sounding/gfs grids/spol/radarPolar/qc1/moments/sband/corrected	grids/spol/radarPolar/qc1/rate/sband/v1.0	Read in corrected moments, and temperature profile from GFS, compute PID and precip rate. This produces our final v1.0 data set.	4.1
run_FixFieldVals.biasCompute.sur	FixFieldVals.biasCompute.sur	grids/spol/radarPolar/field/moments/sband/sur grids/spol/radarPolar/qc1/moments/sband/corrected/sur	features/qc1/fieldBias/sur	See section 7. Use FixFieldVals to compare the files between the field data and qc1 data, to compute the corrections that have been applied in the QC1 processing. These corrections are then saved in SPDB.	4.2
run_FixFieldVals.biasApply.rhi1	FixFieldVals.biasApply.rhi1	features/qc1/fieldBias/sur grids/spol/radarPolar/field/moments/sband/rhi	grids/spol/radarPolar/qc1/moments/sband/corrected/rhi1	See section 7. Read corrections from the previous step (in SPDB) and apply these to the PrecipRhi1 RHIs which have problems. These corrected RHI files must then be manually copied into place (using rsync) in the final data set.	4.2
run_SpdxXml2Table.field_bias.sur	SpdxXml2Table.field_bias.sur	features/qc1/fieldBias/sur	features/qc1/fieldBias/tables	Convert SPDB data to a comma-delimited ASCII table.	4.2

Script name	Param file(s)	Input dir(s)	Output dir	Comments	Section
run_PlotFieldBias.sur		features/qc1/fieldBias/tables		Plot field biases. Figure 4.1.	4.2
run_CreateSpolImages.sband.qc1		grids/spol/radarPolar/qc1/rate/sband/v1.0/sur	images/spol_moments/qc1/v1.0	Create quick-look images for surveillance scans.	4.3
run_CreateSpolMovies.sband.qc1		images/spol_moments/qc1/v1.0	images/spol_movies/qc1/v1.0	Create quick-look movies for surveillance scans.	4.3

7. References

- Bringi, V. N. and V. Chandrasekar, 2001: Polarimetric Doppler Weather Radar, Principles and Applications. *Cambridge University Press*. ISBN-13 978-0-521-01955-2.
- Cocks, S. B., and Coauthors, 2019: A Prototype Quantitative Precipitation Estimation Algorithm for Operational S-Band Polarimetric Radar Utilizing Specific Attenuation and Specific Differential Phase. Part II: Performance Verification and Case Study Analysis. *J. Hydrometeor.*, 20, 999–1014, <https://doi.org/10.1175/JHM-D-18-0070.1>.
- Dixon, M., J.C. Hubbert, 2012: The Separation of Noise and Signal Components in Doppler RADAR Returns. ERAD 2012, The Seventh European Conference on RADAR in Meteorology and Hydrology. Toulouse, France. [SP-078](#).
- Dixon, M., WC Lee, R.A. Rilling, C. Burghart, J. VanAndel 2016: CfRadial Data File Format. Version 1.3. <http://opensky.library.ucar.edu/collections/OSGC-000-000-021-355> <https://opensky.ucar.edu/islandora/object/manuscripts%3A838>, <https://github.com/NCAR/CfRadial/blob/master/docs/CfRadialDoc.v1.5.20211201.pdf>
- Doviak, R.J., D.S. Zrnica, 1993. Doppler Radar and Weather Observations. Academic Press, 2nd ed. ISBN-13: 978-0122214226
- Gorgucci, E., Scarchilli, G and Chandrasekar, V.: A procedure to calibrate multi-parameter weather radar using properties of the rain medium. *IEEE Trans. Geosci. Remote Sens.*, 17, 269-276, 1999.
- Hubbert, J., V. N. Bringi, 1995: An Iterative Filtering Technique for the Analysis of Copolar Differential Phase and Dual-Frequency Radar Measurements. *J. Atmos. Oceanic Technol.*, 12, 643-648. doi: [http://dx.doi.org/10.1175/1520-0426\(1995\)012<0643:AIFTFT>2.0.CO;2](http://dx.doi.org/10.1175/1520-0426(1995)012<0643:AIFTFT>2.0.CO;2)
- Hubbert, J. C., V. N. Bringi and D. Brunkow, 2003: Studies of the Polarimetric Covariance Matrix. Part I: Calibration Methodology. . *J. Atmos. Technol.*, Vol 20, May, 696 - 706.
- Hubbert, J., V. Chandrasekar, V. N. Bringi, P. Meischner, 1993: Processing and Interpretation of Coherent Dual-Polarized Radar Measurements. *J. Atmos. Oceanic Technol.*, 10, 155-164. doi: [http://dx.doi.org/10.1175/1520-0426\(1993\)010<0155:PAIOCD>2.0.CO;2](http://dx.doi.org/10.1175/1520-0426(1993)010<0155:PAIOCD>2.0.CO;2)
- Hubbert, J. C., M. Dixon, S. M. Ellis, G. Meymaris, 2009: Weather Radar Ground Clutter. Part I: Identification, Modeling, and Simulation. *J. Atmos. Oceanic Technol.*, 26, 1165-1180. doi: <http://dx.doi.org/10.1175/2009JTECHA1159.1>
- Hubbert, J. C., M. Dixon, S. M. Ellis, 2009: Weather Radar Ground Clutter. Part II: Real-Time Identification and Filtering. *J. Atmos. Oceanic Technol.*, 26, 1181-1197. doi: <http://dx.doi.org/10.1175/2009JTECHA1160.1>
- Hubbert, J.C., M. Dixon, G. Meymaris, and S.M. Ellis, 2022: The effects of temperature on Zdr calibration, 37th Conference on Radar Meteorology, Norman, OK, Sept., paper 13B.1, 16 pages.
- Jameson, A. R., E. A. Mueller, 1985: Estimation of Propagation-Differential Phase Shift from Sequential Orthogonal Linear Polarization Radar Measurements. *J. Atmos. Oceanic Technol.*, 2, 133-137. doi: [http://dx.doi.org/10.1175/1520-0426\(1985\)002<0133:EOPDPS>2.0.CO;2](http://dx.doi.org/10.1175/1520-0426(1985)002<0133:EOPDPS>2.0.CO;2)
- Melnikov, V., and D. Zrnica, 2015: Monitoring radar Zdr calibration using ground clutter. 37th Conference on Radar Meteorology, Norman, OK, Sept. Paper 10.3.
- Seliga, T. A., V. N. Bringi, 1976: Potential Use of Radar Differential Reflectivity Measurements at Orthogonal Polarizations for Measuring Precipitation. *J. Appl. Meteor.*, 15, 69-76. doi: [http://dx.doi.org/10.1175/1520-0450\(1976\)015<0069:PUORDR>2.0.CO;2](http://dx.doi.org/10.1175/1520-0450(1976)015<0069:PUORDR>2.0.CO;2)
- Sirmans, D., and B. Urell, 2001: On Measuring WSR88D antenna gain using solar flux. *NWS Radar Operations Center, report*.

- Steiner, Matthias, James A. Smith, 2002: Use of Three-Dimensional Reflectivity Structure for Automated Detection and Removal of Non Precipitating Echoes in Radar Data. *J. Atmos. Oceanic Technol.*, **19**, 673-686. doi: [http://dx.doi.org/10.1175/1520-0426\(2002\)019<0673:UOTDRS>2.0.CO;2](http://dx.doi.org/10.1175/1520-0426(2002)019<0673:UOTDRS>2.0.CO;2)
- Vivekanandan, J., G. Zhang, S. M. Ellis, D. Rajopadhyaya, S.K. Avery, 2003: Radar reflectivity calibration using differential propagation phase measurement. *Radio Science*, Vol. 38. No. 3, 8049.
- Vivekanandan, J., S. M. Ellis, R. Oye, D.S. Zrnice, A. V. Ryzhkov and J. Straka, 1999: Cloud microphysics retrieval using S-band dual-polarization radar measurements. *Bull. Amer. Meteor. Soc.*, 80, 381 – 388.
- Wilson, Damian R., Anthony J. Illingworth, T. Mark Blackman, 1997: Differential Doppler Velocity: A Radar Parameter for Characterizing Hydrometeor Size Distributions. *J. Appl. Meteor.*, **36**, 649-663. doi: <http://dx.doi.org/10.1175/1520-0450-36.6.649>
- Zrnice, D.S.; Balakrishnan, N.; Sachidananda, M., 1988: Processing And Interpretation Of Alternately Polarised Weather Radar Echoes. Geoscience and Remote Sensing Symposium, 1988. IGARSS '88. Remote Sensing: Moving Toward the 21st Century., International Volume: 1 Page(s): 243-246. doi: [10.1109/IGARSS.1988.570103](http://dx.doi.org/10.1109/IGARSS.1988.570103)